Proceedings of Proceedings of the International Design Engineering Technical Conferences & Computers & Information in Engineering Conference
IDETC/CIE 2021
August 17-20, 2021, Virtual Conference, USA

IDETC2021-67821

MULTI-MATERIAL TOPOLOGY OPTIMIZATION OF FERROMAGNETIC SOFT ROBOTS USING RECONCILED LEVEL SET METHOD

Jiawei Tian[1], **Xianfeng David Gu**[2,3], **Shikui Chen**[1,*]
Department of Mechanical Engineering[1]
Department of Computer Science[2]
Department of Applied Mathematics & Statistics[3]
State University of New York at Stony Brook,
Stony Brook, New York, USA, 11794
Email: {Jiawei.Tian, Shikui.Chen}@stonybrook.edu
Gu@cs.stonybrook.edu

ABSTRACT

Ferromagnetic soft materials can generate flexible mobility and changeable configurations under an external magnetic field. They are used in a wide variety of applications, such as soft robots, compliant actuators, flexible electronics, and bionic medical devices. The magnetic field enables fast and biologically safe remote control of the ferromagnetic soft material. The shape changes of ferromagnetic soft elastomers are driven by the ferromagnetic particles embedded in the matrix of a soft elastomer. The external magnetic field induces a magnetic torque on the magnetized soft material, causing it to deform. To achieve the desired motion, the soft active structure can be designed by tailoring the layouts of the ferromagnetic soft elastomers. This paper aims to optimize multi-material ferromagnetic actuators. Multi-material ferromagnetic flexible actuators are optimized for the desired kinematic performance using the reconciled level set method. This type of magnetically driven actuator can carry out more complex shape transformations by introducing ferromagnetic soft materials with more than one magnetization direction. Whereas many soft active actuators exist in the form of thin shells, the newly proposed extended level set method (X-LSM) is employed to perform conformal topology optimization of ferromagnetic soft actuators on the manifolds. The objective function comprises two sub-objective functions, one for the kinematic requirement and the other for minimal compliance. Shape sensitivity analysis is derived using the material time derivative and the adjoint variable method. Three examples are provided to demonstrate the effectiveness of the proposed framework.

1 INTRODUCTION

The increasing use of flexible active materials in the production of robots has been going on for more than a decade. The next generation of robots, known as soft robotics, has opened up a broad range of applications, including bionic medical devices, flexible wearable devices, and collaborative industrial machines [1, 2, 3, 4, 5, 6]. Soft robots can produce flexible movements and alter shapes with the flexible material [7]. This differs considerably from traditional rigid-body robots, where motion is transmitted by the relative position change of rigid components. The adaptability and flexibility of soft robots enable high-level motion behavior such as bending, stretching, twisting, walking, or even their combinations.

Among the various active materials, magnetically responsive matters are distinguished by their rapid response to the input signals and their ability to be controlled remotely [8]. Thanks to their biological-friendly interaction and low cost, magnetic soft matters have become a promising tool in the bio-medical field. Moreover, compared with other environmental stimuli such

*Address all correspondence to this author.

as the electric field [9], the acoustic field [10] and the optical field [11], the magnetic field is able to generate relatively higher forces and torques [12, 13, 14]. The higher manipulation forces and torques make it possible to control both macroscopic objects and microscopic particles such as cells, viruses, and even nanoparticles [15, 16, 6].

To achieve the deformation of magnetically actuated materials, a popular approach is to embed magnetic particles into the soft elastomer matrix. Hard magnetic particles, like ferromagnetic particles, are usually selected to be embedd into soft materials. An extraordinary feature of hard magnetic particles is that they retain their residual magnetization even when the applied magnetic field is withdrawn [17]. Due to this residual magnetization, the fast and convoluted shape transformation can be achieved [18, 19]. Before the ferromagnetic soft elastomer is exposed to a strong magnetic field, the ferromagnetic particles are randomly dispersed in the soft elastomer, and there is no net magnetization. When an external magnetic field is applied, a magnetic torque is generated. This torque bends the soft material into a new configuration, forcing the magnetic directions of the hard magnetic particles to be parallel to those of the applied magnetic field. [20].

Research on the design and fabrication of soft robots is still at its infancy and relatively underdeveloped, with increasing efforts in recent years. The review on soft robots could by no means be exhaustive in this paper. For a complete review on the recent development of soft robots, please be referred to [4]. For the sake of brevity, we report only the most representative and relative work of this study. Kim et al. [18, 21] proposed a fabrication technique by reorienting the direction of the ferromagnetic particles during the printing process. The resulting designs with intricate patterns of ferromagnetic materials can achieve a complex morphing form. Diller et al. [8] provided a completely different fabrication solution by encoding hard magnetic particles in an elastomer matrix cured by ultra-violet lithography. Lum [22] devised a programming method to automatically calculate the magnetization and magnetic field required for a flexible magnetic beam to reach the desired shapes.

Besides geometry, the material also plays a key role in the behavioral performance of soft robots [4]. Thanks to the advanced multi-material additive manufacturing technology, magnetic soft robots with multiple constituent materials provide more attractive features. Kokkinis et al. [23] built a magnetically multi-material 3D printing platform to fabricate heterogeneous functional materials consisting of rigid materials, soft swelling materials, as well as elastomer with embedded magnetic particles. Wang et al. [24] designed a nano-composite magnetic actuator comprising a magnetic actuation unit and a geometry determining unit so that various actuating configurations such as bending, elongation, or compressing can be programmed in a single block via erasing the preceding actuation geometry. Using multi-material 3D printing technology, Ji et al. [25] integrated magnetic responsive material and non-responsive materials into a single soft actuator.

Although these magnetically controlled robots are well built to achieve the desired function, they are the product of intuitions, experiences, and biological inspiration [4]. Soft robotics researchers are facing challenges due to the absence of a systematic method for automating the design process. Topology optimization is a promising methodology for the design of soft robots and some attempts have been done up to now. For the sake of brevity, only some works concerning the topology optimization of magnetic actuators are elaborated here. Park et al. [26, 27] designed a lighter magnetic actuator with maximal magnetic energy using level-set-based topology optimization. Park et al. [28] also employed the level set method to design a ferromagnetic actuator , which can achieve the maximum actuating force with limited usage of ferromagnetic material. Also, Li et al. [29] proposed a toolkit to design an electromagnetic actuator to achieve maximal magnetic force based on genetic algorithm and differential evolutionary algorithm. These studies focused primarily on optimizing magnetic energy or magnetic force rather than kinematic performance. Recently, Tian et al. [30, 31] employed the conformal topology optimization on manifolds using the extended level set method and this optimization method was verified on a flytrap gripper.

Geometry and material, two perpetual theme in soft robots design, drive soft robots' behavioral performance in response to the environmental stimuli. Multi-material topology optimization provides a promising avenue to guide our design of soft robots in both material and geometry aspects. Zhang et al. [32, 33] integrated soft actuating material and hard elastic material into one soft finger to achieve maximal bending deflection without sacrifice of carrying capacity. Hiller and Jonathan [34] optimized the distribution of hard and rigid material in a cantilever beam so as to program the predefined profiles. Subramanian et al. [35] implemented topology optimization to design the actuator composed of soft and rigid polymers and a magnetic polymer composite that responds to a magnetic field. Also, a 4D printing gripper consisting of active and passive material is designed to match the given target displacement by virtue of the density-based topology optimization method [36].

Inspired by the variable stiffness laminate (VSL) [37, 38], where the fiber orientation is spatially varied, the multi-material ferromagnetic actuators with multiple magnetic directions will be designed in this study. In addition, designing this kind of ferromagnetic actuators with multiple magnetization orientations also takes the fabrication technology into consideration. Stereolithography will be adopted to fabricate our optimized designs owing to its special characteristic. During the printing process, the light projector can emit the UV light on the selected region of the substrate and this region could be the one constituent phase with certain magnetization direction.

In this study, the reconciled level-set method is employed

to design ferromagnetic soft structures. It is worth noting that the structure is stimulated by a magnetic field which results in a magnetic body force (see Section.2 in detail). It turns this optimization problem into a design-dependent problem since the magnetic load varies as the design evolves during the optimization process [39]. Besides, the newly proposed extended level set method (X-LSM) [40] and conformal mapping theory [41,42] are employed to carry out multi-material topology optimization of a actuator on manifold.

The remaining of the paper is organized as follows: Section.2 introduces the actuation mechanism of ferromagnetic soft material. Section.3 presents details on the multi-material topology optimization for ferromagnetic soft actuators, including the conventional level set method, reconciled level set method, X-LSM with conformal mapping theory, problem formulation, and shape sensitivity analysis, followed by three numerical examples given in Section.4. Section.5 concludes the paper and outlines future work.

2 FERROMAGNETIC SOFT ACTUATORS

In this section, we briefly recapitulate the actuation mechanism of the ferromagnetic soft material and present the governing equations of magnetism. For more details,interested readers are referred to [43].

Firstly, consider an external magnetic field $\boldsymbol{H}$ generated by a pair of electromagnetic coils in air. According to the Biot–Savart law, the resultant magnetic flux density $\boldsymbol{B}^*$ at position $\boldsymbol{x}$ in 3D-space generated by a current I due to the electromagnetic coils can be calculated as

$$\boldsymbol{B}^*(\boldsymbol{x}) = \frac{\mu_0}{4\pi}\int_C \frac{I d\boldsymbol{l}\times\boldsymbol{r}}{|\boldsymbol{r}|^3}, \tag{1}$$

where $d\boldsymbol{l}$ is the differential element vector along the coil path C, pointing to the current direction. $\boldsymbol{r}$ is the displacement from the differential element to the position $\boldsymbol{x}$. μ_0 denotes the air permeability. In the current-free space, the Maxwell's equations governing a static magnetic field are given by

$$\boldsymbol{B}^* = \mu_0 \boldsymbol{H}, \tag{2a}$$
$$curl(\boldsymbol{H}) = 0. \tag{2b}$$

Next, we introduce a ferromagnetic soft elastomer with remnant magnetization $\boldsymbol{M}$ to be placed in a certain region of the current-free space. Based on the physical observation [44], the magnetic flux density $\boldsymbol{B}$ of the ferromagnetic soft material is linearly related to the applied magnetic field $\boldsymbol{H}$ when the field strength is far below the coercivity of the embedded ferromagnetic particles [17], which can be expressed as

$$\boldsymbol{B} = \mu_0(\boldsymbol{H}+\boldsymbol{M}). \tag{3}$$

Hence, the Maxwell equations governing the magnetic field within this magnetic elastomer are defined as

$$\nabla\cdot\boldsymbol{B} = 0, \tag{4a}$$
$$curl\left(\frac{1}{\mu_0}\boldsymbol{B}-\boldsymbol{M}\right) = 0. \tag{4b}$$

Then, the magnetic potential energy of ferromagnetic soft material can be defined as

$$W = -\boldsymbol{M}\cdot\boldsymbol{B}^*. \tag{5}$$

Finally, the magnetic torque τ is derived from the magnetic potential energy as follows:

$$\tau = -\frac{dW}{d\theta} = \boldsymbol{M}\times\boldsymbol{B}^*, \tag{6}$$

where θ is the angle between the vectors of magnetization and applied magnetic flux density. It is noted that this magnetic field should be uniform since the magnetic torques only generate in the uniform magnetic field.

For generality, we consider a nonuniform magnetic field in this paper. The torque caused by a uniform magnetic field is equivalently replaced with a magnetic body force to stimulate the ferromagnetic soft material. The magnetic body force $\boldsymbol{F}_m$ is calculated as [13, 22]

$$\boldsymbol{F}_m = \mu_0(\boldsymbol{M}\cdot\nabla)\boldsymbol{H}. \tag{7}$$

Rewriting the magnetic force with index notation results in the following scalar-valued function of the magnetic force:

$$F_{mi} = \mu_0\left(M_x\frac{\partial H_i}{\partial x}+M_y\frac{\partial H_i}{\partial y}+M_z\frac{\partial H_i}{\partial z}\right), \tag{8}$$

where H_i is the component of magnetic field intensity in the ith direction; M_x, M_y and M_z are the components of magnetization in x, y, and z direction respectively.

From Eq. (3) and Eq. (7), it is noted that the magnetic field and the mechanics field are coupled bilaterally. Specifically, the emergence of the ferromagnetic soft material will disturb the external magnetic field, which in turn affects the force applied to

the ferromagnetic soft material. To simplify the problem, we assume that the existence of a ferromagnetic soft structure does not significantly alter the external magnetic field. Correspondingly, a mutual-coupling model is transformed into a one-way coupling model.

3 MULTI-MATERIAL TOPOLOGY OPTIMIZATION OF FERROMAGNETIC SOFT ACTUATORS

3.1 Classical Level Set Method

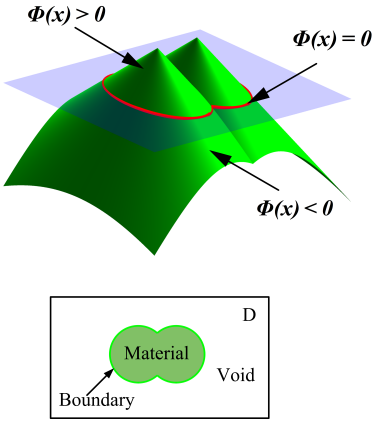

FIGURE 1: A schematic of level set representation.

Conventionally, the level set function Φ is a Lipschitz continuous real-valued function defined in $\mathbb{R}^2$ or $\mathbb{R}^3$ [45]. The boundary of the design $\partial\Omega$ is implicitly represented as the zero level set of the function Φ, as illustrated in Fig. 1. According to the sign of the level set function, the design domain can be divided into three parts, indicating the material, the interface, and the void, respectively. The level-set representation can be formulated as equation (9):

$$\begin{cases} \Phi(x,t) > 0, & x \in \Omega, & \text{material} \\ \Phi(x,t) = 0, & x \in \partial\Omega, & \text{boundary} \\ \Phi(x,t) < 0, & x \in D/\Omega, & \text{void} \end{cases} \tag{9}$$

where D represents the design domain. The dynamics of the boundary evolution is governed by the Hamilton-Jacobi equation:

$$\frac{\partial\Phi(x,t)}{\partial t} - V_n|\nabla\Phi(x,t)| = 0, \tag{10}$$

where V_n is the normal velocity field.

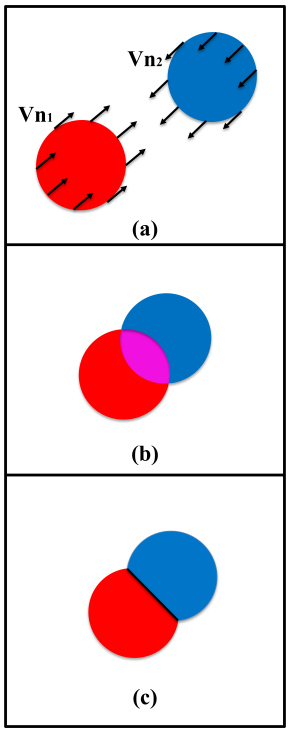

FIGURE 2: Schematic of the reconciled level set method. (a) Two materials moving in opposite directions at the same speed; (b) Overlapped materials; (c) Reconciled level set with MBO operator applied.

3.2 Reconciled Level Set Method for Multi-material Topology Optimization

In this study, the reconciled level set method is employed for topology optimization of ferromagnetic soft actuators. The 'color' level set method [46,47] and the reconciled level set(RLS) method [48, 49, 50] are the two main approaches being widely used to design multi-material structure within the level set framework. The 'color' level set method uses the combined signs of n level set function to represent up to 2^n materials. Whereas the reconcile level set method utilizes a separate signed-distance level set function to represent each material individually. Thus, the n reconciled level set functions can represent n phases, providing a direct relationship between the level set function and the material phase. However, changes in each level set function may result in overlaps between different material phases. This issue can be addressed by applying the Merriman-Bence-Osher (MBO) operator [51, 52] to the level set function for each material phase i:

$$\widetilde{\Phi_i} = 0.5\left(\Phi_i^* - \max_{i\neq j}\Phi_j^*\right), \tag{11}$$

where Φ_i^* represents the level set after evolution and $\widetilde{\Phi_i}$ is the level set function after applying MBO operator. The subscripts i and j denote the different materials.

Fig. 2 is plotted to clearly illustrate the boundary evolution process of two level set functions representing two constituent materials. At first, the red and blue circles lie at a certain distance. Represented by two independent level set functions, the red and blue circles are moving toward one the other at their own speed V_{n1} and V_{n2} before intersecting and overlapping together. With the MBO operator applied, a clear boundary emerges between the two coupled level set functions.

With the reconciled level set method, the interpolated properties $\boldsymbol{D}^*$ with k constituent materials can be expressed as

$$\boldsymbol{D}^* = \sum_{j=1}^{k} H(\Phi_j)\boldsymbol{D}_j + \prod_{j=1}^{k}(1-H(\Phi_j))\boldsymbol{D}_0, \tag{12}$$

where $\boldsymbol{D}_j$ represents the material properties of $j\,th$ constituent and $H(\Phi_j)$ is the Heaviside function of the level set function Φ_j. $\boldsymbol{D}_0$ denotes the dummy material properties. The symbol $\boldsymbol{D}$ represents the material properties and it can be Young's modulus, magnetization or density. According to Eq.8, the interpolated magnetic body force F_{mi}^* with k constituent materials can be calculated as

$$\begin{aligned} F_{mi}^* = \mu_0 &\left(\sum_{j=1}^{k} H(\Phi_j)\boldsymbol{M}_j\cdot\boldsymbol{e}_x + \prod_{j=1}^{k}(1-H(\Phi_j))\boldsymbol{M}_0\cdot\boldsymbol{e}_x\right)\frac{\partial H_i}{\partial x} \\ + \mu_0 &\left(\sum_{j=1}^{k} H(\Phi_j)\boldsymbol{M}_j\cdot\boldsymbol{e}_y + \prod_{j=1}^{k}(1-H(\Phi_j))\boldsymbol{M}_0\cdot\boldsymbol{e}_y\right)\frac{\partial H_i}{\partial y} \\ + \mu_0 &\left(\sum_{j=1}^{k} H(\Phi_j)\boldsymbol{M}_j\cdot\boldsymbol{e}_z + \prod_{j=1}^{k}(1-H(\Phi_j))\boldsymbol{M}_0\cdot\boldsymbol{e}_z\right)\frac{\partial H_i}{\partial z}, \end{aligned} \tag{13}$$

where $\boldsymbol{M}_j$ represents the magnetization of $j\,th$ constituent material and $\boldsymbol{M}_0$ denotes the magnetization of the dummy material. $\boldsymbol{e}_x$, $\boldsymbol{e}_y$ and $\boldsymbol{e}_z$ denote the three unit base vectors in a three-dimensional Cartesian space.

3.3 Conformal Topology Optimization on Manifolds using Extended Level Set Methods (X-LSM)

Many bionic soft actuators exist as curved thin-shell structures or manifolds in a mathematical term. The conventional level set method only works in the Euclidean space where the distance between two points is the length of a line segment between these two points. How to implement level-set-based conformal topology optimization on a manifold, where the shortest path between two points is the geodesic between them, is an important but challenging issue. The problem of level-set-based conformal topology optimization was recently touched upon by Chen & Gu et al. [40, 53] by proposing an extended level set method (X-LSM) using the conformal mapping theory [41, 42].

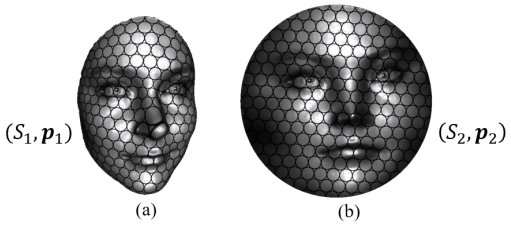

FIGURE 3: Conformal mapping from the 3D surface to the 2D disk preserves infinitesimal circles. (a) infinitesimal circles on a 3D surface. (b) infinitesimal circles on a 2D disk.

The characteristic of conformal mapping is that it conserves shapes and angles locally. As shown in Fig.3, the shape of the infinitesimal circles on the surface is well preserved on a 2D disk after mapping. Conformal mapping provides the point-to-point relationship between the manifold and the 2D plane in the Euclidean space [54].

Using conformal mapping theory, we can conformally parameterize the manifold onto a 2D rectangular domain. The design is equivalently evolved on the 2D plane using the modified Hamilton-Jacobi equation transformed by conformal mapping as follows [40]:

$$\frac{\partial\Phi(x,t)}{\partial t} - e^{-\lambda}V_n|\nabla\Phi(x,t)| = 0, \tag{14}$$

where the λ is the *conformal factor* quantifying the scaling and rotating effect of the conformal mapping. In this way, X-LSM can transform a conformal topology optimization problem on a Riemannian manifold in 3D space into a 2D topology optimization problem in Euclidean space. It is worth noting that only with the conformal mapping can we reach such a concise formulation of the extended level set equation on the manifold, which might otherwise be extraordinarily complex and daunting.

3.4 Problem Formulation

Ferromagnetic soft robots can deliver desired kinematic behaviors by shape morphing. Meanwhile, the robot itself should have enough rigidity to sustain the force when interacting with objects. In this case, the least square approach widely used in compliant mechanisms design [46, 45, 55, 56] is chosen as the sub-objective function for the kinematic requirement. The stiffness at the end effector is used to characterize the rigidity. Therefore, the design issue can be formulated as a balance between the

desired kinematic requirement and structural stiffness as follows:

$$\begin{aligned} \textit{Minimize:} \quad J =& w_1 \left(\int_\Omega \boldsymbol{g} \cdot \boldsymbol{u} \mathrm{d}\Omega + \int_{\Gamma_N} \boldsymbol{f} \cdot \boldsymbol{u} \mathrm{d}s \right) \\ &+ w_2 \left(\int_\Omega k |\, \boldsymbol{u} - \boldsymbol{u}_0|^2 \mathrm{d}\Omega \right)^{\frac{1}{2}}, \\ \textit{Subject to:} \quad & a(\boldsymbol{u},\boldsymbol{v}) = l(\boldsymbol{v}), \quad \forall \boldsymbol{v} \in U \\ & V(\Omega) = V^*, \end{aligned} \tag{15}$$

where U stands for the space of kinematically admissible displacement fields [57]; $\boldsymbol{u}_0$ denotes the target displacement field; $\boldsymbol{u}$ denotes the actual displacement field; Ω indicates the material region in the design domain D. The boundary of the design is denoted by Γ, which comprises segments with Neumann boundary condition Γ_N, Dirichlet boundary condition Γ_D, and free boundary $\partial\Omega$. $\boldsymbol{g}$ and $\boldsymbol{f}$ denote the magnetic body force acting on the soft body and the traction force acting on the Neumann boundary Γ_N respectively. $V(\Omega)$ is the volume of the soft body, and V^* is the target volume. Localizing factor k is used to select the area of concern for kinematic performance. w_1 and w_2 are weighting factors for end compliance and kinematic target respectively. Excessive kinematic weighting factor w_2 tends to cause the structure discontinuity during the optimization process, which makes the structure has no loading capability. Thus, the selection of weighting factors follows the principle that the end compliance and the least square error compared to the target displacement have a relatively closer order of magnitude. Here, $a(\boldsymbol{u},\boldsymbol{v}) = l(\boldsymbol{v})$ is the weak form of governing equation. The energy form $a(\boldsymbol{u},\boldsymbol{v})$ and the load form $l(\boldsymbol{v})$ as well as the volume $V(\Omega)$ are defined as

$$a(\boldsymbol{u},\boldsymbol{v}) = \int_\Omega \varepsilon_{ij}^T(\boldsymbol{u}) \mathbb{C}_{ijkl} \varepsilon_{kl}(\boldsymbol{v}) \mathrm{d}\Omega, \tag{16a}$$

$$l(\boldsymbol{v}) = \int_\Omega \boldsymbol{g} \cdot \boldsymbol{v} \mathrm{d}\Omega + \int_{\Gamma_N} \boldsymbol{f} \cdot \boldsymbol{v} \mathrm{d}s, \tag{16b}$$

$$V(\Omega) = \int_D H(\Phi) \mathrm{d}\Omega, \tag{16c}$$

where ε is the second-order linear strain tensor; $\mathbb{C}_{ijkl}$ is a fourth-order elastic stiffness tensor; $H(\Phi)$ represents the Heaviside function.

3.5 Shape Sensitivity Analysis

This section describes how to construct the design velocity field using the material time derivative. The shape sensitivity of this design-dependent optimization problem is derived using the adjoint method. The objective function (15) is connected to the governing equation (16) using the Lagrange multiplier method as follows:

$$L(\boldsymbol{u},\boldsymbol{v}) = J + \lambda \left(a(\boldsymbol{u},\boldsymbol{v}) - l(\boldsymbol{v}) \right), \tag{17}$$

where the λ is a Lagrange multiplier, and $\boldsymbol{v}$ is the adjoint displacement. The material time derivative is utilized to derive the shape sensitivity [45, 58, 57]:

$$\frac{DL(\boldsymbol{u},\boldsymbol{v})}{Dt} = \frac{DJ}{Dt} + \frac{Da(\boldsymbol{u},\boldsymbol{v})}{Dt} - \frac{Dl(\boldsymbol{v})}{Dt}. \tag{18}$$

For conciseness, the derivative of the Lagrangian is directly presented here. For more details, readers are referred to [30, 31].

$$\begin{aligned} \frac{DL(\boldsymbol{u},\boldsymbol{v})}{Dt} =& w_1 \int_\Gamma \boldsymbol{g} \cdot \boldsymbol{u} \boldsymbol{V}_n \mathrm{d}s + \frac{1}{2} w_2 D_0 \int_\Gamma k |\, \boldsymbol{u} - \boldsymbol{u}_0|^2 \boldsymbol{V}_n \mathrm{d}s \\ &+ \int_\Gamma \varepsilon_{ij}(\boldsymbol{u}) \mathbb{C}_{ijkl} \varepsilon_{kl}(\boldsymbol{v}) \boldsymbol{V}_n \mathrm{d}s - \int_\Gamma \boldsymbol{g} \cdot \boldsymbol{v} \boldsymbol{V}_n \mathrm{d}s. \end{aligned} \tag{19}$$

With the steepest descent method, the normal design velocity with the mean curvature κ and the volume constraint can be constructed as

$$\begin{aligned} \boldsymbol{V}_n =& \boldsymbol{g} \cdot \boldsymbol{v} - w_1 \boldsymbol{g} \cdot \boldsymbol{u} - \frac{w_2 D_0}{2} k |\, \boldsymbol{u} - \boldsymbol{u}_0|^2 - \varepsilon_{ij}(\boldsymbol{u}) \mathbb{C}_{ijkl} \varepsilon_{kl}(\boldsymbol{v}) \\ &+ \nu \left(V - V^* \right) + \iota \kappa, \end{aligned} \tag{20}$$

where ν and ι are the Lagrange multipliers for the volume and perimeter constraints; κ is the curvature of the boundary.

4 NUMERICAL EXAMPLES

4.1 Topology Optimization of a Magnetically-Driven Gripper with Two Constituent Materials

The first example is to find the optimum design of a ferromagnetic 2-jaw soft gripper structure. Due to the symmetry, only one jaw is studied. As shown in Fig. 4, each jaw is modelled as a cantilever beam ($2m \times 1m$), with its left side clamped. The interaction between the jaw and the object is modelled as a loading $\boldsymbol{p} = (0,1)\,N$ and a surface friction $\boldsymbol{f} = (1,0)\,N$, distributed on the contacting area as highlighted by the black area. This black area is also selected as the area of concern for kinematic performance. The jaw is actuated by a downward external magnetic field with a magnitude of $10mT$. The Young's modulus of both actuating materials keeps the same and is set to $E = 0.1MPa$. The Poisson's ratio for all materials is set to be 0.3. The magnitudes of the magnetization of both actuating materials are identical with $2.5 \times 10^6 A/m$. The only difference between the two actuating materials is the direction of the magnetization, in which one is set

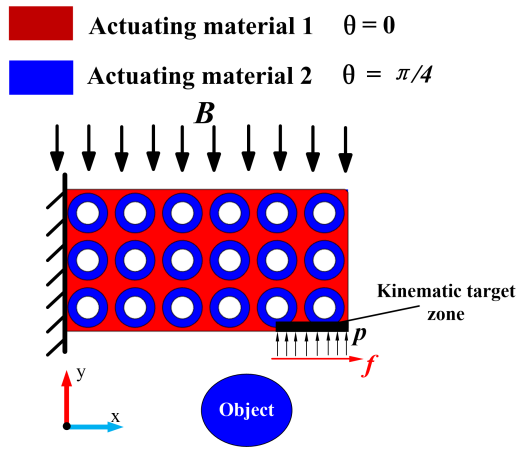

FIGURE 4: Boundary conditions of the multi-material ferromagnetic gripper structure.

to 0° and the other to 45°. As a consequence, the magnetic body force distributions onto the two constituent materials are completely different. To avoid singularity, a dummy material with Young's modulus $E = 10\,Pa$ and magnetization $M = 250A/m$ are set for the void. The target displacement u_{y0} is set to be $-0.25\,m$. The weighting factors for the end compliance and the kinematic target are set as $w_1 = 0.02$ and $w_2 = 0.98$.

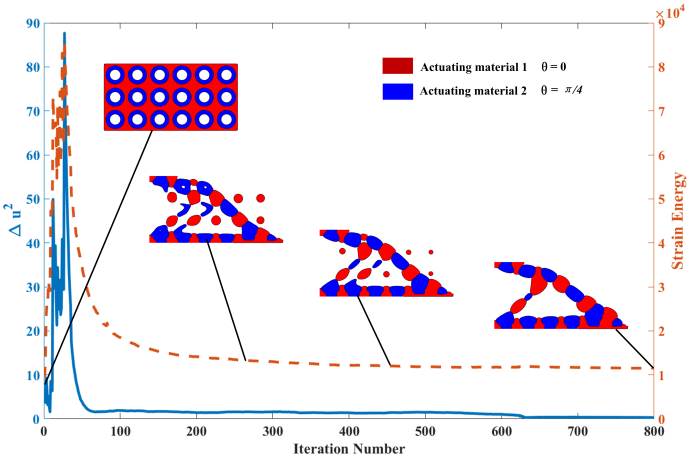

FIGURE 5: The optimization history curves and design evolution of the multimaterial magnetically-driven gripper.

The whole design domain is discretized with 100×50 grids. The volume fractions of the two constituent materials are both constrained at 20%. The converge curve for the optimization process and the design evolution history are shown in Fig. 5. At the end of the topology optimization, the volumes of actuating material 1 and 2 are 19.92% and 20.05%. The least-square error with respect to the target displacement converges to 0.0580. The magnetization orientations in the optimized design and the deformed configuration under the external magnetic field is shown in Fig. 6. We also extrude the 2D design into a 2.5D design to simulate the grasping process. As shown in Fig. 7, two grippers with opposite magnetization directions are mounted symmetrically on a platform. With the actuation of the external magnetic field parallel to the platform, the two jaws bend towards the center to grasp the white object.

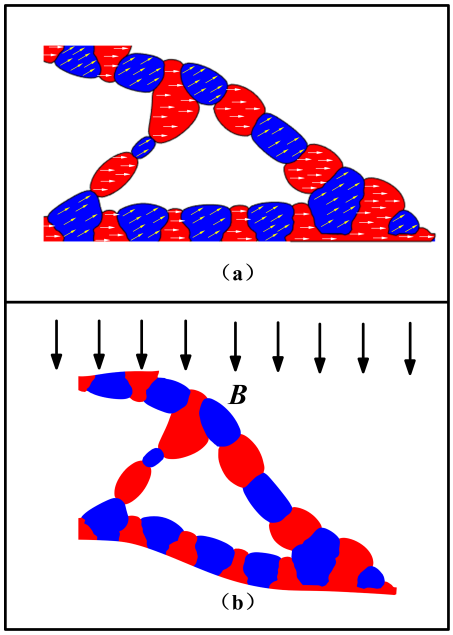

FIGURE 6: The magnetization orientations in one jaw of the optimized gripper and its deformed configuration under the external magnetic field. (a) The magnetization orientations in the multi-material ferromagnetic gripper. (b) The bending configuration of the optimized multi-material ferromagnetic gripper under a downward magnetic field.

4.2 Topology Optimization of a Magnetic Actuator with Three Constituent Materials

The second example is to solve the optimum design of a magnetic actuator with three types of actuating materials. The dimension of design domain is $2\,m \times 1\,m$. The details of boundary conditions are shown in Fig. 8, where two endpoints of the bottom edge are fixed. A loading $\boldsymbol{p} = (0, -1)\,N$ is applied at the contacting area as highlighted by the black area to model the reaction force given by the object. This black area is also se-

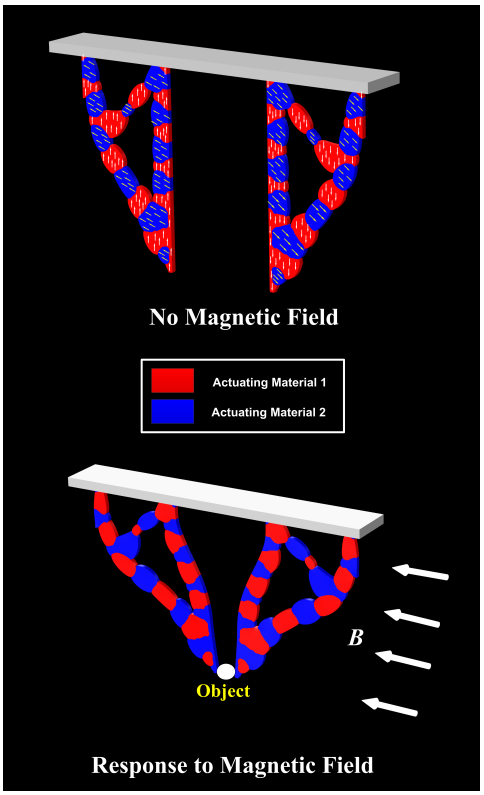

FIGURE 7: Simulation of the grasping process of the two-material ferromagnetic gripper.

lected as the area of concern for kinematic performance. The actuator is controlled by an upward external magnetic field with a magnitude of $10mT$. The Young's modulus of all actuating materials keeps the same and is set as $E = 0.1MPa$. The Poisson's ratio for all materials is set to be 0.3. The magnitudes of the magnetization of three actuating materials are identical with $2.5 \times 10^6 A/m$. The magnetization directions of the three actuating materials are set to 0°, 90° and 180°, respectively. To avoid singularity, a dummy material with Young's modulus $E = 10Pa$ and magnetization $M = 250A/m$ are set for the void. Due to the symmetry, only left half domain is studied. The target displacement u_{y0} is set to be 0.25 m. The weighting factors for the end compliance and the kinematic target are set as $w_1 = 0.05$ and $w_2 = 0.95$.

The whole design domain is discretized with 50×50 grids. The volume fractions of the two constituent materials are both constrained at 20%. The converge curve for the optimization process and the design evolution history are shown in Fig. 9. The volumes of the actuating material 1 and 2 are 19.95% and 20.11% when the optimization ends. The least-square error with respect to the target displacement converges to 0.1958. The magnetization orientations are plotted on the optimized design and

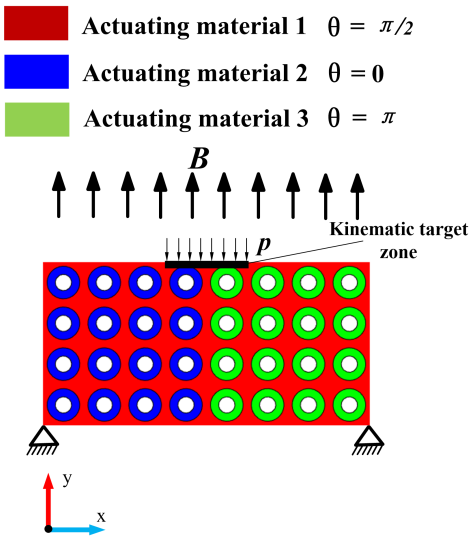

FIGURE 8: Boundary conditions of the three-material magnetic actuator.

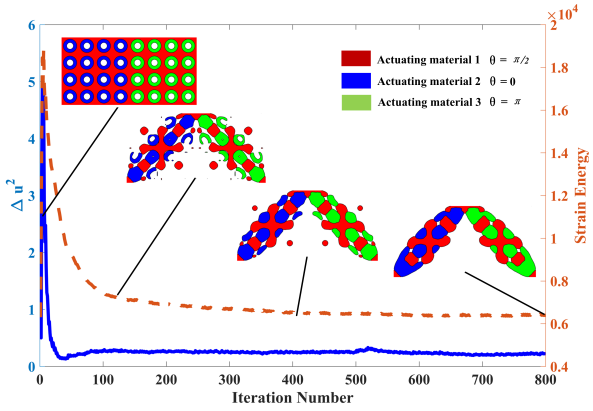

FIGURE 9: The optimization history curve and design evolution of the magnetic driven actuator.

the resultant deformed configuration in response to the external magnetic field is given in Fig. 10. Finally, we extrude the 2D design into a 2.5D design and corresponding deformed configuration is given in Fig.11.

4.3 Conformal Topology Optimization of a Magnetic Driven Flytrap Shell Structure with Two Constituent Materials

The flytrap shell structure with single constituent material has been investigated in our recent work [30]. In this section, X-LSM combined with RLS method is applied to design a multi-material flytrap shell actuator. As shown in Fig.12, the magnetization of the two constituent materials are along the shell geome-

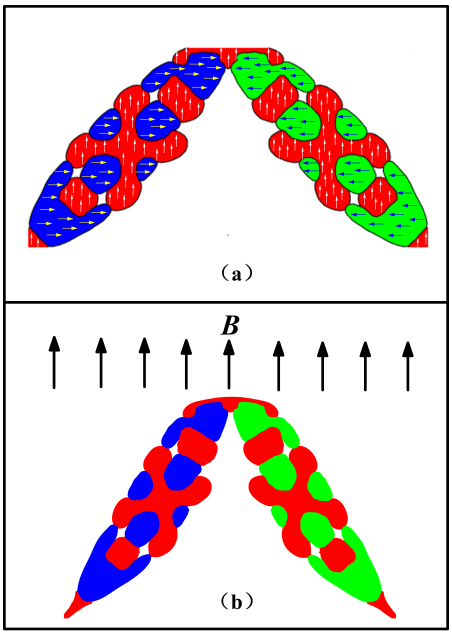

FIGURE 10: (a) The magnetization orientations in the three-material ferromagnetic actuator. (b) The deformed configuration of the optimized three-material ferromagnetic actuator under the external magnetic field.

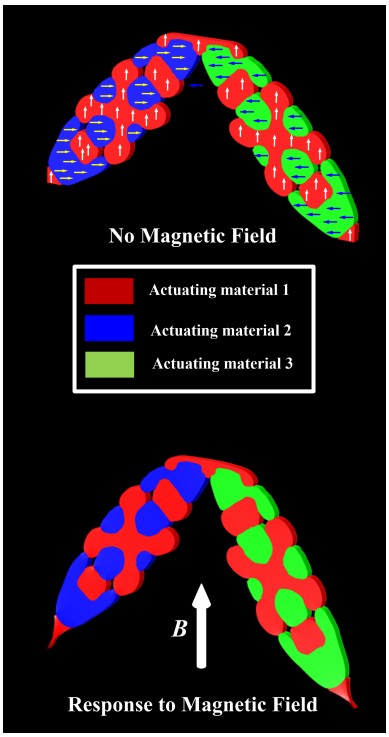

FIGURE 11: Simulation of the behavior of three-material actuator.

try tangent direction $\boldsymbol{t}_1$ (red arrows) and normal direction $\boldsymbol{n}$ (blue arrows), respectively. The volume fraction targets for both materials are 0.45 and 0.25, respectively. The boundary condition for petal shell is also shown in Fig.12, where the bottom edge is fixed and a interaction force $\boldsymbol{F} = (1, 0, -1)\, N$ is applied on the top edge. The blue area is chosen as the area of concern for kinematic performance and the target displacement is set as u_{x0}=$-1\ m$. The weighting factor w_1 and w_2 are set as 0.2 and 0.8. The material properties for both constituent are assumed with a Young's modulus $E = 0.1\,MPa$ and Poisson's ratio $\mu = 0.3$. The magnitudes of both magnetization are identical with $M = 8 \times 10^4\, A/m$. In addition, a dummy material with Young's modulus $E = 10\,Pa$ and magnetization $M = 8\,A/m$ are set for the void.

The span of a single petal is approximately 2.5 m $\times$ 1.6 m and the thickness is 0.05 m. The elastic shell equilibrium equation is solved on the 3D petal surface. The petal surface is meshed with 63318 triangular elements, and the conformal mapped 2D rectangular domain is discretized with 197 $\times$ 501 grids. In the implementation, the top layer of the petal is retained by setting the design velocity to zero. The initial and final designs in the 2D rectangular domain and the petal surface are shown in Fig.14, where the red and blue areas represent the actuating materials with $\boldsymbol{t}_1$ and $\boldsymbol{n}$ magnetic poles, respectively. The optimization curves for minimum compliance and target displacement are plotted in Fig.13. Finally, a flytrap actuator with 6

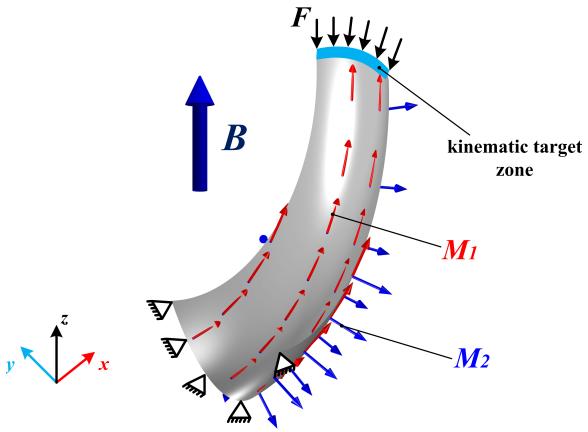

FIGURE 12: Boundary condition of multi-material flytrap shell structure (only one finger).

petals can be constructed by making a circular pattern of the optimized design. Fig.15 is plotted to illustrate the grasping behavior of the design vividly.

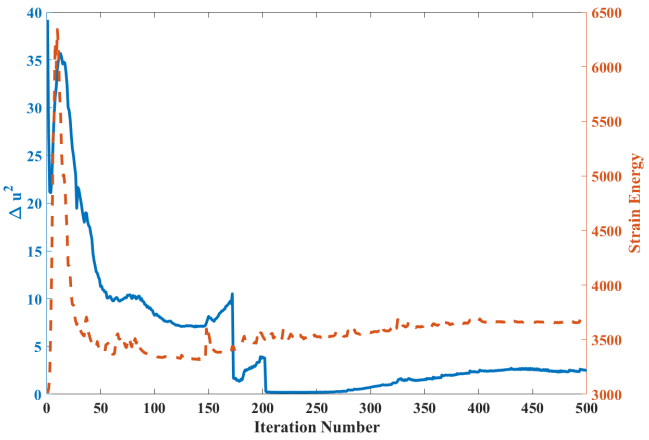

FIGURE 13: The optimization history curve of the multi-material magnetic driven flytrap actuator.

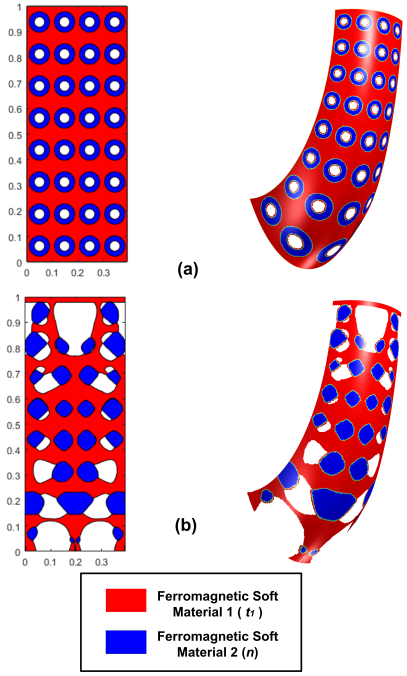

FIGURE 14: The (a)initial and (b) final design of the flytrap shell structure with two constituent materials.

5 CONCLUSION

In this study, ferromagnetic soft actuators with multiple magnetization poles are designed using the reconciled level set method. Magnetic field and mechanics field are coupled in the design models of the multi-material ferromagnetic soft actuator. Magnetic body force is adopted as a non-contact stimulus to control ferromagnetic soft structures. The design problem is recast as a balance of the kinematic performance and load-carrying capability. Three numerical examples are provided to verify the performance of the proposed approach.

One of our future efforts will focus on the nonlinear topology optimization of ferromagnetic soft actuators to capture their mechanical behavior more precisely. With the help of the stereolithographic 3D manufacturing technology, our optimized multi-material ferromagnetic soft actuators are being fabricated for further experimental validation.

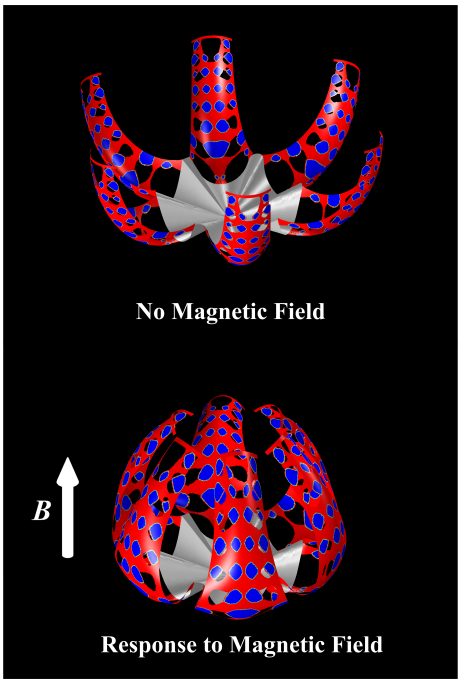

FIGURE 15: Simulation of the grasping process of the multi-material flytrap shell actuator.

ACKNOWLEDGMENT

The authors gratefully acknowledge financial support from the National Science Foundation (CMMI-1762287), the Ford University Research Program (URP) (Award No. 2017-9198R), and the State University of New York (SUNY) at Stony Brook. The authors would like to sincerely thank Prof. Xuanhe Zhao at MIT for the insightful discussions and also for providing the Abaqus code for ferromagnetic material modeling.

REFERENCES

[1] Majidi, C. "Soft robotics: a perspective—current trends and prospects for the future". *Soft robotics,* ***1***(1), pp. 5–11.

[2] Rus, D., and Tolley, M. T. "Design, fabrication and control of soft robots". *Nature,* ***521***(7553), pp. 467–475.

[3] Cianchetti, M., Laschi, C., Menciassi, A., and Dario, P. "Biomedical applications of soft robotics". *Nature Reviews Materials,* ***3***(6), pp. 143–153.

[4] Chen, F., and Wang, M. Y. "Design Optimization of Soft Robots: A Review of the State of the Art". *IEEE Robotics & Automation Magazine*.

[5] Zarek, M., Layani, M., Cooperstein, I., Sachyani, E., Cohn, D., and Magdassi, S. "3D printing of shape memory polymers for flexible electronic devices". *Advanced Materials,* ***28***(22), pp. 4449–4454.

[6] Zhao, X., Kim, J., Cezar, C. A., Huebsch, N., Lee, K., Bouhadir, K., and Mooney, D. J. "Active scaffolds for on-demand drug and cell delivery". *Proceedings of the National Academy of Sciences,* ***108***(1), pp. 67–72.

[7] Asaka, K., and Okuzaki, H., 2014. *Soft Actuators: Materials, Modeling, Applications, and Future Perspectives*. Springer.

[8] Xu, T., Zhang, J., Salehizadeh, M., Onaizah, O., and Diller, E. "Millimeter-scale flexible robots with programmable three-dimensional magnetization and motions". *Science Robotics,* ***4***(29), p. eaav4494.

[9] Zhang, W., Ahmed, S., Masters, S., Ounaies, Z., and Frecker, M. "Finite element analysis of electroactive polymer and magnetoactive elastomer based actuation for origami-inspired folding". In ASME 2016 Conference on Smart Materials, Adaptive Structures and Intelligent Systems, American Society of Mechanical Engineers, pp. V001T01A001–V001T01A001.

[10] Brunet, T., Merlin, A., Mascaro, B., Zimny, K., Leng, J., Poncelet, O., Aristégui, C., and Mondain-Monval, O. "Soft 3D acoustic metamaterial with negative index". *Nature materials,* ***14***(4), p. 384.

[11] Grier, D. G. "A revolution in optical manipulation". *nature,* ***424***(6950), p. 810.

[12] Ranzoni, A., Janssen, X. J., Ovsyanko, M., van IJzendoorn, L. J., and Prins, M. W. "Magnetically controlled rotation and torque of uniaxial microactuators for lab-on-a-chip applications". *Lab on a Chip,* ***10***(2), pp. 179–188.

[13] Erb, R. M., Martin, J. J., Soheilian, R., Pan, C., and Barber, J. R. "Actuating soft matter with magnetic torque". *Advanced Functional Materials,* ***26***(22), pp. 3859–3880.

[14] Erb, R. M., Jenness, N. J., Clark, R. L., and Yellen, B. B. "Towards holonomic control of Janus particles in optomagnetic traps". *Advanced materials,* ***21***(47), pp. 4825–4829.

[15] Ye, H., Shen, Z., and Li, Y. "Computational modeling of magnetic particle margination within blood flow through LAMMPS". *Computational Mechanics,* ***62***(3), pp. 457–476.

[16] Wang, S., Zhou, Y., Tan, J., Xu, J., Yang, J., and Liu, Y. "Computational modeling of magnetic nanoparticle targeting to stent surface under high gradient field". *Computational mechanics,* ***53***(3), pp. 403–412.

[17] Zhao, R., Kim, Y., Chester, S. A., Sharma, P., and Zhao, X. "Mechanics of hard-magnetic soft materials". *Journal of the Mechanics and Physics of Solids,* ***124***, pp. 244–263.

[18] Kim, Y., Yuk, H., Zhao, R., Chester, S. A., and Zhao, X. "Printing ferromagnetic domains for untethered fast-transforming soft materials". *Nature,* ***558***(7709), p. 274.

[19] Diller, E., Zhuang, J., Zhan Lum, G., Edwards, M. R., and Sitti, M. "Continuously distributed magnetization profile for millimeter-scale elastomeric undulatory swimming". *Applied Physics Letters,* ***104***(17), p. 174101.

[20] Wang, L., Kim, Y., Guo, C. F., and Zhao, X. "Hard-magnetic elastica". *Journal of the Mechanics and Physics of Solids*, p. 104045.

[21] Kim, Y., Parada, G. A., Liu, S., and Zhao, X. "Ferromagnetic soft continuum robots". *Science Robotics,* ***4***(33), p. eaax7329.

[22] Lum, G. Z., Ye, Z., Dong, X., Marvi, H., Erin, O., Hu, W., and Sitti, M. "Shape-programmable magnetic soft matter". *Proceedings of the National Academy of Sciences,* ***113***(41), pp. E6007–E6015.

[23] Kokkinis, D., Schaffner, M., and Studart, A. R. "Multimaterial magnetically assisted 3D printing of composite materials". *Nature communications,* ***6***(1), pp. 1–10.

[24] Wang, L., Razzaq, M. Y., Rudolph, T., Heuchel, M., Nöchel, U., Mansfeld, U., Jiang, Y., Gould, O. E., Behl, M., Kratz, K., et al. "Reprogrammable, magnetically controlled polymeric nanocomposite actuators". *Materials Horizons,* ***5***(5), pp. 861–867.

[25] Ji, Z., Yan, C., Yu, B., Wang, X., and Zhou, F. "Multi-materials 3D printing for free assembly manufacturing of magnetic driving soft actuator". *Advanced Materials Interfaces,* ***4***(22), p. 1700629.

[26] Park, S.-i., and Min, S. "Design of magnetic actuator with nonlinear ferromagnetic materials using level-set based topology optimization". *IEEE Transactions on Magnetics,* ***46***(2), pp. 618–621.

[27] Park, S.-i., Min, S., Yamasaki, S., Nishiwaki, S., and Yoo, J. "Magnetic actuator design using level set based topology optimization". *IEEE Transactions on magnetics,* ***44***(11), pp. 4037–4040.

[28] Park, S.-I., and Min, S. "Magnetic actuator design for maximizing force using level set based topology optimization". *IEEE transactions on magnetics,* ***45***(5), pp. 2336–2339.

[29] Li, Y., Liu, L., Yang, S., Ren, Z., and Ma, Y. "A Multi-Objective Topology Optimization Methodology and its Application to Electromagnetic Actuator Designs". *IEEE Transactions on Magnetics,* ***56***(2), pp. 1–4.

[30] Tian, J., Zhao, X., Gu, X. D., and Chen, S. "Designing ferromagnetic soft robots (FerroSoRo) with level-set-based multiphysics topology optimization". In 2020 IEEE International Conference on Robotics and Automation (ICRA), IEEE, pp. 10067–10074.

[31] Tian, J., Zhao, X., Gu, X. D., and Chen, S. "Designing Conformal Ferromagnetic Soft Actuators Using Extended Level Set Methods (X-LSM)". In International Design Engineering Technical Conferences and Computers and Information in Engineering Conference, Vol. 83990, American Society of Mechanical Engineers, p. V010T10A012.

[32] Zhang, H., Kumar, A. S., Chen, F., Fuh, J. Y., and Wang, M. Y. "Topology Optimized Multimaterial Soft Fingers for Applications on Grippers, Rehabilitation, and Artificial Hands". *IEEE/ASME Transactions on Mechatronics,* ***24***(1), pp. 120–131.

[33] Zhang, H., Kumar, A. S., Fuh, J. Y. H., and Wang, M. Y. "Investigation on developing a topology optimized and 3D printable multimaterial soft gripper". In 2018 IEEE 14th International Conference on Control and Automation (ICCA), IEEE, pp. 692–697.

[34] Hiller, J., and Lipson, H. "Automatic design and manufacture of soft robots". *IEEE Transactions on Robotics,* ***28***(2), pp. 457–466.

[35] Sundaram, S., Skouras, M., Kim, D. S., van den Heuvel, L., and Matusik, W. "Topology optimization and 3D printing of multimaterial magnetic actuators and displays". *Science advances,* ***5***(7), p. eaaw1160.

[36] Geiss, M. J., Boddeti, N., Weeger, O., Maute, K., and Dunn, M. L. "Combined Level-Set-XFEM-Density Topology Optimization of Four-Dimensional Printed Structures Undergoing Large Deformation". *Journal of Mechanical Design,* ***141***(5), p. 051405.

[37] Ghiasi, H., Fayazbakhsh, K., Pasini, D., and Lessard, L. "Optimum stacking sequence design of composite materials Part II: Variable stiffness design". *Composite Structures,* ***93***(1), pp. 1–13.

[38] Boddeti, N., Tang, Y., Maute, K., Rosen, D. W., and Dunn, M. L. "Optimal design and manufacture of variable stiffness laminated continuous fiber reinforced composites". *Scientific reports,* ***10***(1), pp. 1–15.

[39] Deaton, J. D., and Grandhi, R. V. "A survey of structural and multidisciplinary continuum topology optimization: post 2000". *Structural and Multidisciplinary Optimization,* ***49***(1), pp. 1–38.

[40] Ye, Q., Guo, Y., Chen, S., Lei, N., and Gu, X. D. "Topology optimization of conformal structures on manifolds using extended level set methods (X-LSM) and conformal geometry theory". *Computer Methods in Applied Mechanics and Engineering,* ***344***, pp. 164–185.

[41] Gu, X., Wang, Y., Chan, T. F., Thompson, P. M., and Yau, S.-T. "Genus zero surface conformal mapping and its application to brain surface mapping". *IEEE transactions on medical imaging,* ***23***(8), pp. 949–958.

[42] Lui, L. M., Gu, X., Chan, T. F., Yau, S.-T., et al. "Variational method on riemann surfaces using conformal parameterization and its applications to image processing". *Methods and Applications of Analysis,* ***15***(4), pp. 513–538.

[43] Saxena, P. "On the general governing equations of electromagnetic acoustic transducers". *Archive of Mechanical Engineering,* ***60***(2), pp. 231–246.

[44] Bertotti, G., 1998. *Hysteresis in magnetism: for physicists, materials scientists, and engineers*. Gulf Professional Publishing.

[45] Allaire, G., Jouve, F., and Toader, A.-M. "Structural optimization using sensitivity analysis and a level-set method". *Journal of computational physics,* ***194***(1), pp. 363–393.

[46] Wang, M. Y., Chen, S., Wang, X., and Mei, Y. "Design of multimaterial compliant mechanisms using level-set methods".

[47] Wang, M. Y., and Wang, X. ""Color" level sets: a multiphase method for structural topology optimization with multiple materials". *Computer Methods in Applied Mechanics and Engineering,* ***193***(6-8), pp. 469–496.

[48] Chen, S., Gonella, S., Chen, W., and Liu, W. K. "A level set approach for optimal design of smart energy harvesters". *Computer Methods in Applied Mechanics and Engineering,* ***199***(37-40), pp. 2532–2543.

[49] Vogiatzis, P., Chen, S., Wang, X., Li, T., and Wang, L. "Topology optimization of multi-material negative Poisson's ratio metamaterials using a reconciled level set method". *Computer-Aided Design,* ***83***, pp. 15–32.

[50] Jiang, L., Gu, X., and Chen, S. "Generative Design of Bionic Structures via Concurrent Multiscale Topology Optimization & Conformal Geometry Method". *Journal of Mechanical Design*, pp. 1–29.

[51] Merriman, B., Bence, J. K., and Osher, S. J. "Motion of multiple junctions: A level set approach". *Journal of computational physics,* ***112***(2), pp. 334–363.

[52] Zhang, X., Chen, J.-S., and Osher, S. "A multiple level set method for modeling grain boundary evolution of polycrystalline materials". *Interaction and multiscale mechanics,* ***1***(2), pp. 178–191.

[53] Ye, Q., Guo, Y., Chen, S., Gu, X. D., and Lei, N. "Topology optimization of conformal structures using extended level set methods and conformal geometry theory". In ASME 2018 International Design Engineering Technical Conferences and Computers and Information in Engineering Conference, American Society of Mechanical Engineers Digital Collection.

[54] Gu, X. D., and Yau, S.-T., 2008. *Computational conformal geometry*. International Press Somerville, MA.

[55] Allaire, G., and Jouve, F. "Optimal design of micromechanisms by the homogenization method". *Revue Eu-*

ropéenne des Eléments, ***11***(2-4), pp. 405–416.

[56] Sigmund, O. "On the design of compliant mechanisms using topology optimization". *Journal of Structural Mechanics,* ***25***(4), pp. 493–524.

[57] Choi, K. K., and Kim, N.-H., 2006. *Structural sensitivity analysis and optimization 1: linear systems*. Springer Science & Business Media.

[58] Wang, M. Y., Wang, X., and Guo, D. "A level set method for structural topology optimization". *Computer methods in applied mechanics and engineering,* ***192***(1-2), pp. 227–246.